

In Situ Construction of g-C₃N₄/g-C₃N₄ Metal-Free Heterojunction for Enhanced Visible-Light Photocatalysis

Fan Dong,^{*,†} Zaiwang Zhao,[†] Ting Xiong,[†] Zilin Ni,[†] Wendong Zhang,[‡] Yanjuan Sun,[†] and Wing-Kei Ho[§]

[†]Chongqing Key Laboratory of Catalysis and Functional Organic Molecules, College of Environmental and Biological Engineering, Chongqing Technology and Business University, Chongqing 400067, China

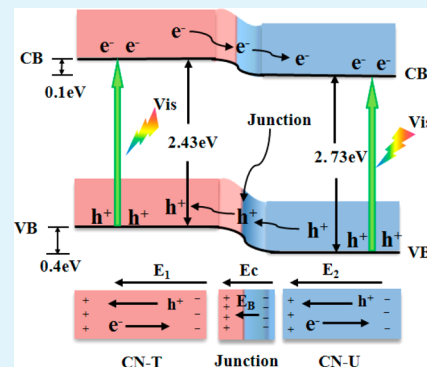
[‡]College of Urban Construction and Environmental Engineering, Chongqing University, Chongqing 400045, China

[§]Department of Science and Environmental Studies, The Centre for Education in Environmental Sustainability, The Hong Kong Institute of Education, Hong Kong, China

Supporting Information

ABSTRACT: The photocatalytic performance of the star photocatalyst g-C₃N₄ was restricted by the low efficiency because of the fast charge recombination. The present work developed a facile in situ method to construct g-C₃N₄/g-C₃N₄ metal-free isotype heterojunction with molecular composite precursors with the aim to greatly promote the charge separation. Considering the fact that g-C₃N₄ samples prepared from urea and thiourea separately have different band structure, the molecular composite precursors of urea and thiourea were treated simultaneously under the same thermal conditions, in situ creating a novel layered g-C₃N₄/g-C₃N₄ metal-free heterojunction (g-g CN heterojunction). This synthesis method is facile, economic, and environmentally benign using easily available earth-abundant green precursors. The confirmation of isotype g-g CN heterojunction was based on XRD, HRTEM, valence band XPS, ns-level PL, photocurrent, and EIS measurement. Upon visible-light irradiation, the photogenerated electrons transfer from g-C₃N₄ (thiourea) to g-C₃N₄ (urea) driven by the conduction band offset of 0.10 eV, whereas the photogenerated holes transfer from g-C₃N₄ (urea) to g-C₃N₄ (thiourea) driven by the valence band offset of 0.40 eV. The potential difference between the two g-C₃N₄ components in the heterojunction is the main driving force for efficient charge separation and transfer. For the removal of NO in air, the g-g CN heterojunction exhibited significantly enhanced visible light photocatalytic activity over g-C₃N₄ alone and physical mixture of g-C₃N₄ samples. The enhanced photocatalytic performance of g-g CN isotype heterojunction can be directly ascribed to efficient charge separation and transfer across the heterojunction interface as well as prolonged lifetime of charge carriers. This work demonstrated that rational design and construction of isotype heterojunction could open up a new avenue for the development of new efficient visible-light photocatalysts.

KEYWORDS: carbon nitride, visible light photocatalysis, metal free heterojunction, molecular composite precursors, photoelectrochemical, charge separation and transfer, band offset



1. INTRODUCTION

Visible-light photocatalysis has attracted intensive interest, as it provides a green and potential route for the wide applications in clean energy production, environmental remediation, and final chemical synthesis.^{1–10} Seeking highly active photocatalysts has been a worldwide continuing endeavor.^{1–10} In general, the photocatalytic performance is mainly governed by the intrinsic physicochemical properties of semiconductors, including band gap structure, surface electronic structure, surface area and pore structure, and morphology.^{2–6} The band gap structure, determining the band position, light absorption spectra, and charge transfer of semiconductors, is a dominant factor.^{3,11} So far, various types of visible light photocatalysts have been developed, which can be divided into four types depending on their composition and band gap structure, including metal-/non-metal-doped semiconductors with large band gap,^{12–14}

metal containing semiconductors with narrow band gap,^{15–18} plasmonic noble metals,^{19,20} and more recently discovered metal-free semiconductors.^{21–23}

The polymeric graphitic C₃N₄ (g-C₃N₄) made of earth abundant elements is of particular interest. It is first discovered as visible light photocatalyst by Wang et al.²¹ In general, the g-C₃N₄ can be prepared by pyrolysis of nitrogen-rich precursors, such as cyanamide, Dicyandiamide, trithiocyanuric acid, melamine, triazine, heptazine derivatives, and more recently discovered urea and thiourea.^{24–34} However, the photocatalytic performance of g-C₃N₄ has been restricted by the low efficiency, mainly due to the fast charge recombination.^{6–8}

Received: August 28, 2013

Accepted: October 21, 2013

Published: October 21, 2013



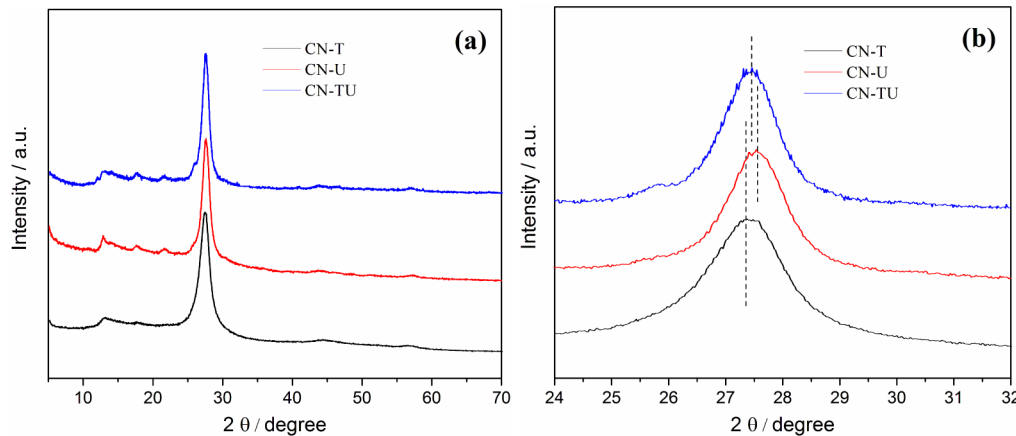


Figure 1. (a) XRD patterns of CN-T, CN-U, and CN-TU, and (b) enlarged profile of the dominant (002) peak.

To improve the photocatalytic performance of $\text{g-C}_3\text{N}_4$, researchers have developed various strategies to address this issue, including mesostructure introduction, nanostructure engineering, semiconductor compositing, noble metal deposition, and metal/non-metal doping.^{6–8,35,36} It is important to note that the polymeric nature of $\text{g-C}_3\text{N}_4$ facilitates the tuning of its band gap structure by simply using different precursors, variation of pyrolysis conditions and doping. The reported band gap energies of $\text{g-C}_3\text{N}_4$ range from 2.4 to 2.8 eV depending on the different preparation conditions.^{24–36}

The band alignment of two semiconductors with well-matched band structure is generally employed to promote the separation of charge at the interfaces of two semiconductors, subsequently reducing charge recombination. In the photocatalysis field, the construction of intimate heterojunction between two appropriate semiconductors is an effective strategy to enhance the photocatalytic performance.^{37–46} Several kinds of $\text{g-C}_3\text{N}_4$ -based heterojunctions have been developed by coupling $\text{g-C}_3\text{N}_4$ with other types of inorganic photocatalysts.^{37–46} Successful examples include inorganic–organic heterojunctions of graphene/ $\text{g-C}_3\text{N}_4$, Au/ $\text{g-C}_3\text{N}_4$, TiO_2 / $\text{g-C}_3\text{N}_4$, MoS_2 / $\text{g-C}_3\text{N}_4$, TaON/ $\text{g-C}_3\text{N}_4$, ZnO / $\text{g-C}_3\text{N}_4$, Bi_2WO_6 / $\text{g-C}_3\text{N}_4$, CdS/ $\text{g-C}_3\text{N}_4$, WO_3 / $\text{g-C}_3\text{N}_4$, and BiOBr/ $\text{g-C}_3\text{N}_4$.^{37–46} The development of these heterojunctions relied largely on the extra well-matched semiconductors.

Recently, this band alignment strategy was further advanced by constructing phase heterojunctions between two different crystal phases of a single semiconductor, such as anatase-rutile phase TiO_2 heterojunction,^{47,48} α - β -phase Ga_2O_3 heterojunction,⁴⁹ and α - β -phase Bi_2O_3 heterojunction.⁵⁰ Wang et al prepared CNS-CN isotype heterojunctions with enhanced visible-light activity by coating the precursor onto the surface of presynthesized $\text{g-C}_3\text{N}_4$ followed with further thermal treatment.⁵¹ The slight differences in the band structure between two different phases enable the formation of anisotype/isotype nanojunctions at the interface of different components, leading to the enhanced photocatalytic activity of these heterojunctions arising from promoted charge separation.

Taking into account the fact that the band gap structure of $\text{g-C}_3\text{N}_4$ can be simply tuned by using different precursors, coupling two components of $\text{g-C}_3\text{N}_4$ with well-matched band structure forming a $\text{g-C}_3\text{N}_4/\text{g-C}_3\text{N}_4$ isotype heterojunction can provide an alternative novel pathway to address the intrinsic drawbacks of $\text{g-C}_3\text{N}_4$ for enhanced photocatalysis without relying on extra semiconductors. For intimate electronic

coupling between the two components of isotype $\text{g-C}_3\text{N}_4$, molecular composite precursors consisting of two different precursors for $\text{g-C}_3\text{N}_4$ can be employed. To the best of our knowledge, there is little report on the synthesis of $\text{g-C}_3\text{N}_4/\text{g-C}_3\text{N}_4$ metal-free heterojunction at molecular level.

Previous work showed that $\text{g-C}_3\text{N}_4$ samples prepared from urea and thiourea separately had different band gap energies.^{30–32} The easily available urea and thiourea were considered as green precursors for $\text{g-C}_3\text{N}_4$. In the present work, the molecular composite precursors consisting of urea and thiourea were prepared and treated simultaneously under the same thermal conditions, in situ creating a novel $\text{g-C}_3\text{N}_4/\text{g-C}_3\text{N}_4$ metal-free heterojunction (g-g CN heterojunction). The g-g CN heterojunction exhibited significantly enhanced visible light activity for removal of NO in air over $\text{g-C}_3\text{N}_4$ alone and physical mixture of $\text{g-C}_3\text{N}_4$ samples. The enhanced photocatalytic performance is shown to be ascribed to the efficient charge separation and transfer across the heterojunction interface, and increased lifetime of photoinduced charge carriers. The present work demonstrated that rational design and construction of isotype heterojunction is an effective strategy for the development of efficient visible-light photocatalysts. Furthermore, the synthesis method is facile, economic, and environmentally benign, and thus it is highly attractive for large scale environmental and energetic applications.

2. EXPERIMENTAL SECTION

2.1. Construction of $\text{g-C}_3\text{N}_4/\text{g-C}_3\text{N}_4$ Metal-Free Heterojunction. All chemicals used in this study were analytical grade and were used without further treatment. In a typical synthesis, 6 g of thiourea, and 6 g of urea were dissolved with 30 mL water in an alumina crucible. The solution of urea and thiourea were then dried at 60 °C overnight to get the molecular composite precursors. The molecular composite precursors in semiclosed alumina crucible with a cover were heated to 550 °C at a heating rate of 15 °C min⁻¹ in a muffle furnace and maintained for 2 h. After the reaction, the alumina crucible was cooled down to room temperature. The resultant $\text{g-C}_3\text{N}_4/\text{g-C}_3\text{N}_4$ metal-free heterojunction (g-g CN heterojunction) was collected for further use. The gases generated during the condensation process were absorbed by dilute alkaline solution. For comparison, 12 g of thiourea and 12 g of urea were treated separately under the same thermal conditions. The prepared $\text{g-C}_3\text{N}_4$ samples were named as CN-T, CN-U, and CN-TU according to the precursors of thiourea, urea, and thiourea–urea composite used in the synthesis process, respectively. Physical mixture of CN-T and CN-U was also prepared as reference and named CN-mixture. Figure 1 illustrated the in situ formation

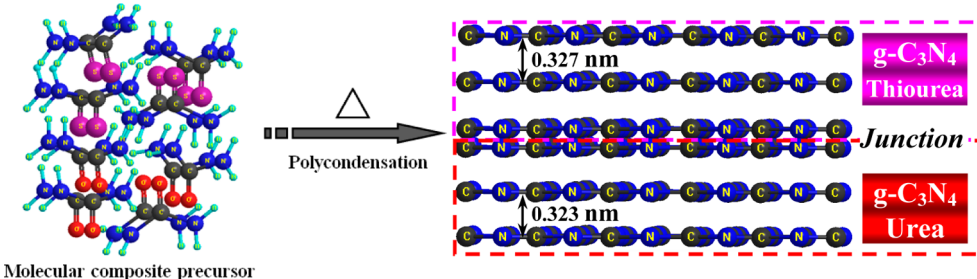


Figure 2. Schematic illustration of the in situ formation process and the atomic structure of the CN-T/CN-U heterojunction from molecular composite precursors consisting of thiourea and urea.

process of the CN-T/CN-U isotype heterojunction with molecular composite precursors of thiourea and urea. For comparison, 6 g of thiourea and 6 g of urea were mechanically mixed and the resulted mixture was treated at 550 °C for 2 h. This sample was named as CN-TU-mech.

2.2. Structural Characterization Methods. The crystal phase was analyzed by X-ray diffraction with Cu $\text{K}\alpha$ radiation (XRD model D/max RA, Japan) at a scan rate of 0.01° $2\theta/\text{s}$. The scan range of 2θ was 5–80°. The morphology and structure were examined by transmission electron microscopy (TEM: JEM-2010, Japan). FT-IR spectra were recorded on a Nicolet Nexus spectrometer on samples embedded in KBr pellets. The UV-vis diffuse reflection spectra were obtained for the dry-pressed disk samples using a Scan UV-vis spectrophotometer (UV-vis DRS UV-2450, Shimadzu, Japan) equipped with an integrating sphere assembly, using BaSO₄ as reflectance sample. Nitrogen adsorption–desorption isotherms were obtained on a nitrogen adsorption apparatus (ASAP 2020, USA) with all samples degassed at 150 °C for 12 h prior to measurements. The photoluminescence spectra were measured with a fluorescence spectrophotometer (F-7000, Japan) using a Xe lamp as excitation source with optical filters. Time-resolved photoluminescence (PL) spectroscopy was recorded on FLsp920 Fluorescence spectrometer (Edinburgh Instruments) with excitation at 420 nm. The photocurrent measurement were conducted on a CHI 660B electrochemical system (Shanghai, China) using a standard three-electrode cell with a working electrode, a platinum wire counter electrode, and a standard calomel electrode (SCE) reference electrode. Na₂SO₄ (0.5 M) was used as the electrolyte solution. The working electrode was prepared according to the following process. Twenty milligrams of as-prepared sample was suspended in 0.5 mL of DMF, which was then dip-coated on a 10 mm × 20 mm indium–tin oxide (ITO) glass electrode. The electrode was then annealed at 350 °C for 1 h at a heating rate 6 °C/min. Visible-light irradiation was provided by MVL-210 with a UV cutoff filter. Electrochemical impedance spectroscopy (EIS) was carried out at the open-circuit potential. A sinusoidal ac perturbation of 5 mV was applied to the electrode over the frequency range 0.05 to 1×10^5 Hz.

2.3. Evaluation of Visible Light Photocatalytic activity. The photocatalytic activity was investigated by removal of NO at ppb levels in a continuous flow reactor at ambient temperature. The volume of the rectangular reactor, made of stainless steel and covered with Saint-Glass, was 4.5 L (30 cm × 15 cm × 10 cm). A 150 W commercial tungsten halogen lamp was vertically placed outside the reactor. A UV cutoff filter (420 nm) was adopted to remove UV light in the light beam.

For each photocatalytic activity test, two sample dishes (with a diameter of 12.0 cm) containing photocatalyst powders were placed in the center of the reactor. The weight of the photocatalyst used for each dish was kept at 0.1 g. The 0.1 g sample was added into 30 mL of H₂O and ultrasonicated for 10 min. Then the aqueous suspension was coated onto the glass dishes. The coated dish was pretreated at 60 °C to remove water in the suspension and then cooled to room temperature before photocatalytic testing.

The NO gas was acquired from a compressed gas cylinder at a concentration of 100 ppm of NO (N₂ balance, standard gas). The initial concentration of NO was diluted to about 600 ppb by the air

stream. The desired relative humidity (RH) level of the NO flow was controlled at 50% by passing the zero air streams through a humidification chamber. The gas streams were premixed completely by a gas blender, and the flow rate was controlled at 2.4 L/min by a mass flow controller. After the adsorption–desorption equilibrium was achieved, the lamp was turned on. The concentration of NO was continuously measured by a chemiluminescence NO analyzer (Thermo Environmental Instruments Inc., 42i-TL), which monitors NO_x and NO₂ with a sampling rate of 1.0 L/min. The removal ratio (η) of NO was calculated as $\eta (\%) = (1 - C/C_0) \times 100\%$, where C and C₀ are concentrations of NO in the outlet steam and the feeding stream, respectively.

3. RESULTS AND DISCUSSION

3.1. Confirmation of g-C₃N₄/g-C₃N₄ Metal-Free Heterojunction. The XRD patterns of CN-T, CN-U and CN-TU are presented in Figure 1a. The XRD patterns confirmed the formation of graphitic stacking C₃N₄ layers.²⁰ Two peaks are observed in the XRD patterns for g-C₃N₄ samples prepared from thiourea, urea and molecular composite of thiourea and urea. The peak observed at 13.1° indexed as the (100) plane corresponds to the in-plane structural packing motif of tristiazine units. This calculated distance is 0.675 nm corresponding to the hole-to-hole distance in the nitride pores. Another intense peak around 27.5° corresponds to the interlayer stacking of aromatic units of CN with an interlayer distance of 0.324 nm, ascribing to the (002) plane of the stacking of the conjugated aromatic system.²⁰ Figure 1b suggests that the diffraction angle of (002) peak for CN-U (27.6°) is higher than that of CN-T (27.3°) probably due to the additional leaving motif oxygen in urea that facilitates the condensation process and enables structural perfection.⁵² The interlayer distances of CN-T and CN-U are calculated to be 0.327 and 0.323 nm, indicating that the crystal structure of CN-U is in a denser packing fashion. Further observation of Figure 1b indicates that the diffraction angle (002) peak of CN-TU is located between CN-T and CN-U, confirming the formation of CN-T/CN-U heterostructure. The molecular structure of this CN-T/CN-U heterojunction is illustrated in Figure 2. It can be seen that the electronic interconnection between the CN-T and CN-U takes place at the atomic level because of the use of molecular composite precursors. For 1 g of thiourea and urea, the g-C₃N₄ yield was 0.074 and 0.032 g, respectively. On the basis of this data, the percentage of CN-T and CN-U in the g-C₃N₄/g-C₃N₄ heterojunction was determined to be 69.8 and 30.2%. This relative ratio of CN-T/CN-U is similar to that of rutile TiO₂/anatase TiO₂ in the well-known P25 with phase junction.

The successful construction of the CN-T/CN-U heterojunction is further demonstrated by the TEM images in Figure 3. Figure 3a shows that the CN-T is composed of large dense

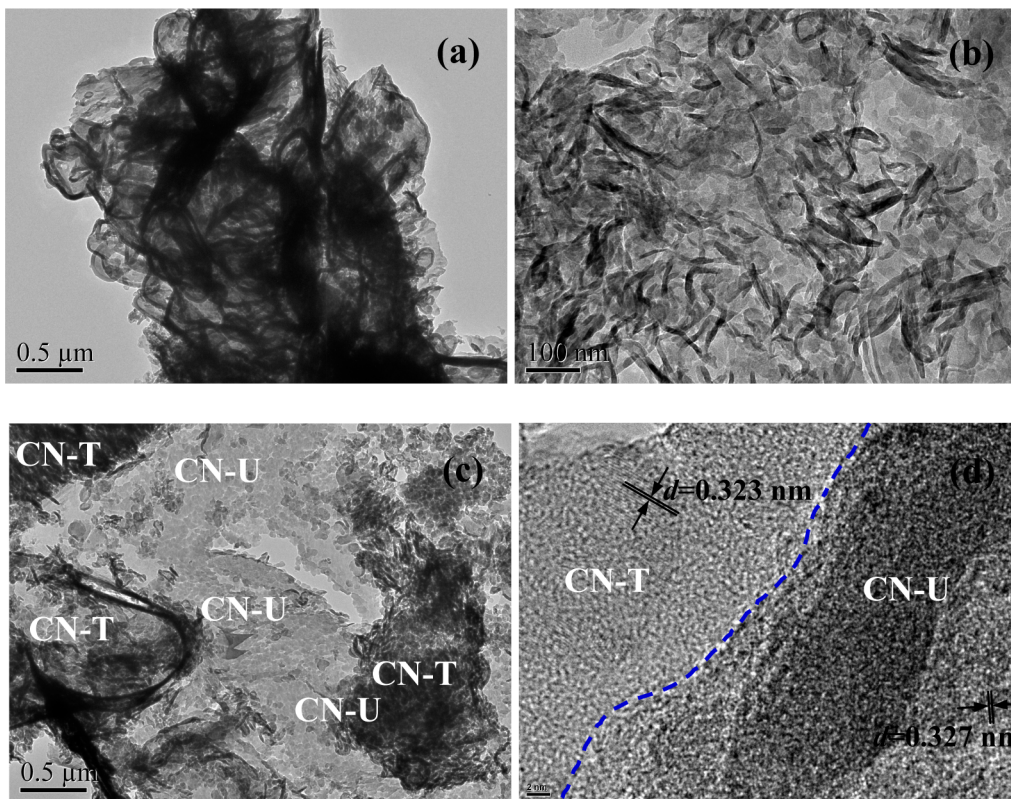


Figure 3. TEM images of (a) CN-T, (b) CN-U, and (c, d) CN-TU.

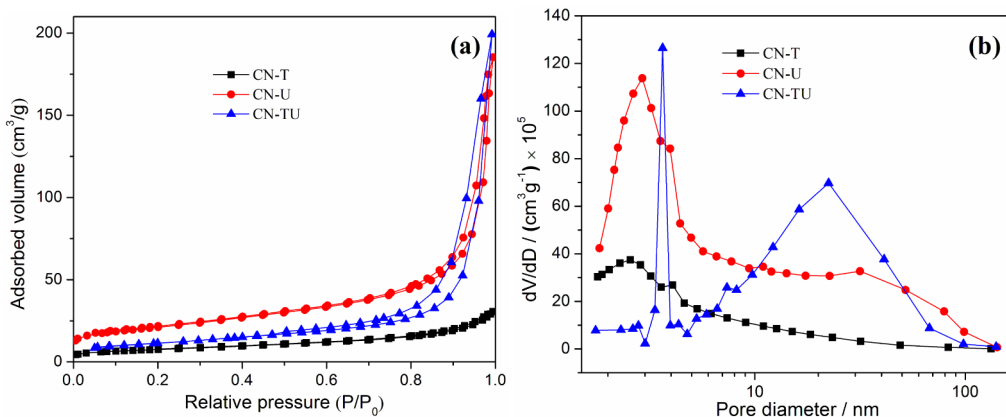


Figure 4. (a) N_2 adsorption–desorption isotherms and (b) the corresponding pore-size distribution curves of CN-T, CN-U, and CN-TU.

thick layers, whereas the CN-U consist smooth paper-fold thinner sheets (Figure 3b), similar to the morphology of graphene nanosheets. Figure S1 in the Supporting Information shows the SEM images of CN-T and CN-U. It can be seen that the $\text{g-C}_3\text{N}_4$ from thiourea is composed of bulk and dense thick layers, whereas $\text{g-C}_3\text{N}_4$ from urea consist porous thinner sheets. The morphologic difference between CN-T and CN-U is distinctive, which is also consistent with TEM images (Figure 3a, b). The urea and thiourea have different molecular structure. The heteroatoms, oxygen in urea and sulfur in thiourea, play a very important role in the processing of carbon nitride condensation and formation of nanostructures. As a result, the $\text{g-C}_3\text{N}_4$ samples prepared from neat thiourea and urea have significantly different morphology because of the different condensation processes. This difference makes the identification of CN-T and CN-U in the CN-TU hetero-

structure possible. Figure 3c shows the morphology of CN-TU. It can be seen that the dense and thick CN-T layers are found packing closely onto surface of graphene-like CN-U thin sheets, both of which are integrated together as a heterostructure, resulting in the formation of CN-T/CN-U hybrids. To provide more solid evidence for the confirmation of heterojunction, an HRTEM image in the interface of CN-T/CN-U hybrids is taken and shown in Figure 3d. The interface is located between the thick CN-T layer and thin CN-U layer. The d values of lattice spacing are measured to be 0.327 and 0.323 nm, matching with the spacing of the (002) crystal planes of CN-T and CN-U in the composites. This result indicates the hybridization of CN-T and CN-U in the composite sample, which is also consistent with XRD result.

The nitrogen adsorption–desorption isotherms and Barrett–Joyner–Halenda (BJH) pore-size distribution curves of CN-T,

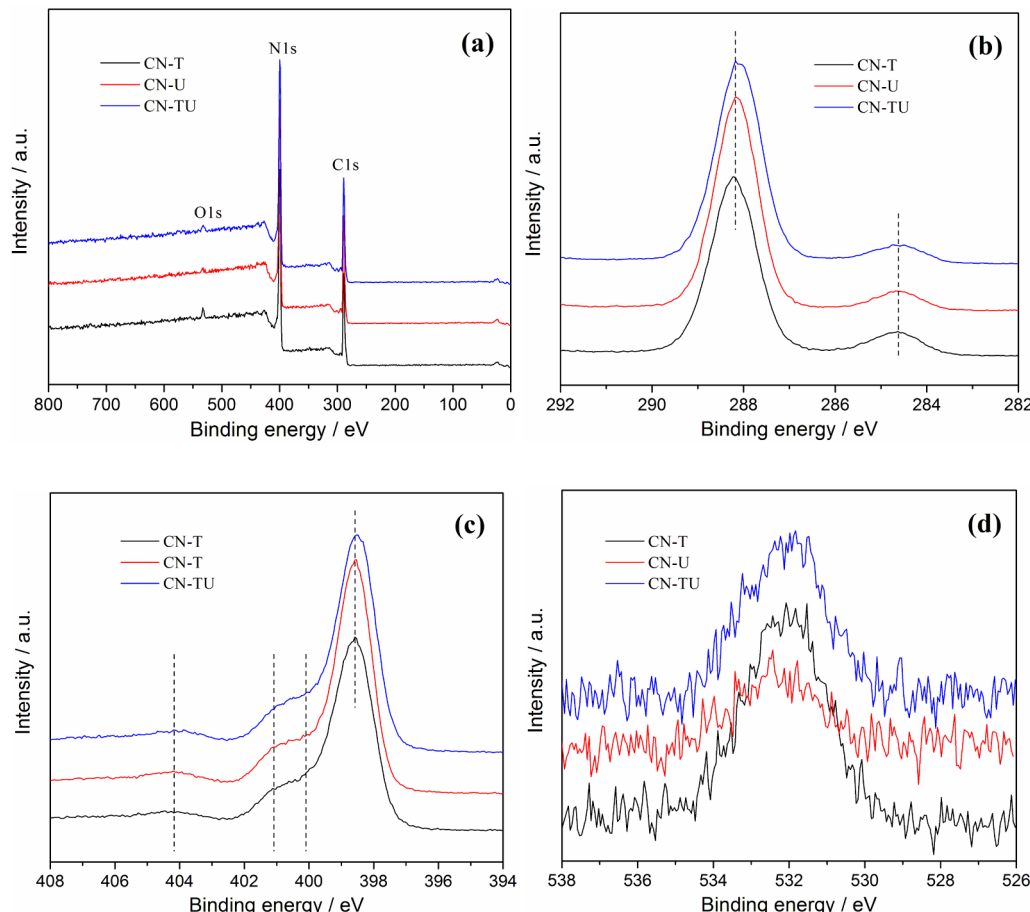


Figure 5. XPS spectra of CN-T, CN-U, and CN-TU, (a) survey, (b) C1s, (c) N1s, and (d) O1s.

CN-U and CN-TU are displayed in Figure 4. The adsorption–desorption isotherms in Figure 4a show that all the samples are of type IV (BDDT Classification), suggesting the presence of mesopores (2–50 nm).⁵³ Compared with CN-T, the hysteresis loop of CN-U shifts to the region of lower pressure and the area of the hysteresis loop becomes large, indicating the formation of relative large mesopores. The hysteresis loop of CN-TU is changed accordingly with the introduction of urea in the precursor. The hysteresis loops are of type H3, which suggests the formation of slit-shaped pores arising from the aggregation of platelike particles.⁵³ This result is in close agreement with the TEM observations of sheetlike morphology (Figure 3). The pore size distribution (PSD) of the samples (Figure 4b) further confirms the formation of mesopores. As can be seen for CN-U sample, the PSD curve is quite broad (from 2 to 100 nm) with small mesopores (~2.9 nm) and large mesopores (~31.6 nm). The small mesopores may reflect porosity within the nanoscale layers and the large mesopores are associated to the pores formed between packed layers. For CN-T sample, only small mesopores (~2.6 nm) can be observed, which also is consistent with TEM image (Figure 3). The CN-TU sample has bimodal mesopores of (3.6 and 22.4 nm) due to the hybridization of CN-T and CN-U. Of all the photocatalysts, CN-U shows the highest BET surface areas of 75 m²/g, whereas CN-T and CN-TU have surface areas of 27 and 41 m²/g. It was found that the additional oxygen in the urea is beneficial for enlarging the surface area of g-C₃N₄, presumably because of the formation of CO₂ during the condensation to suppress the advance of grain boundary.⁵²

3.2. Chemical Composition. Figure S2 in the Supporting Information shows the FT-IR spectra of CN-T, CN-U, and CN-TU. It can be seen that all the g-C₃N₄ samples have absorption bands in the region 800–880 cm⁻¹ corresponding to breathing mode of the triazine units. The peaks observed at 1200–1480 cm⁻¹ are assigned to the typical vibrations C–N heterocycles associated with skeletal stretching vibrations of aromatic rings. The peaks observed in the region of 1570–1640 cm⁻¹ is mainly due to the presence of C=N bonds. The broad band in the range 3000–3600 cm⁻¹ can be ascribed to the uncondensed amine groups and surface adsorbed water molecules.^{30–32}

The XPS measurements were carried out to determine the chemical state of the elements of samples. Figure 5a represents the full survey spectra of CN-T, CN-U, and CN-TU and signals of C, N and O elements are displayed. No peak assigned to S species can be observed for CN-T and CN-TU, indicating the sulfur in thiourea was released during heating treatment. The C1s spectra in Figure 5b represent two peaks at the binding energies of 284.8 and 288.1 eV, respectively. The peak located at 284.8 eV is assigned to adventitious carbon species, and the peak at 288.1 eV is assigned to the tertiary carbon C-(N)₃ in the g-C₃N₄ lattice.^{30–32} The N1s region in Figure 5c can be fitted into four peaks, which can be ascribed to C–N–C (398.8 eV), tertiary nitrogen N-(C)₃ (400.1 eV), N–H groups (401.2 eV), and π-excitations (404.3 eV), respectively.^{30–32} Figure 5d represents the O 1s peak at 532 eV which is assigned to the adsorbed H₂O on the catalyst surface.

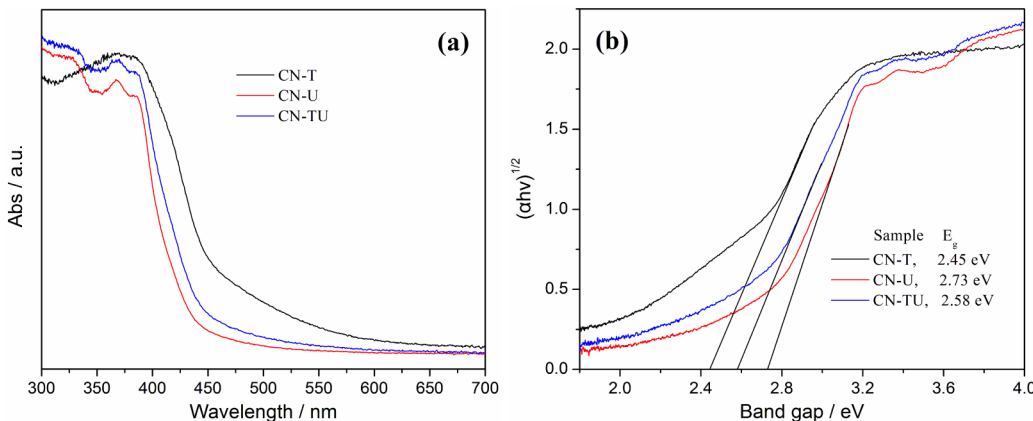


Figure 6. UV-vis DRS (a) and plots of $(\alpha h\nu)^{1/2}$ vs photon energy (b) of CN-T, CN-U and CN-TU.

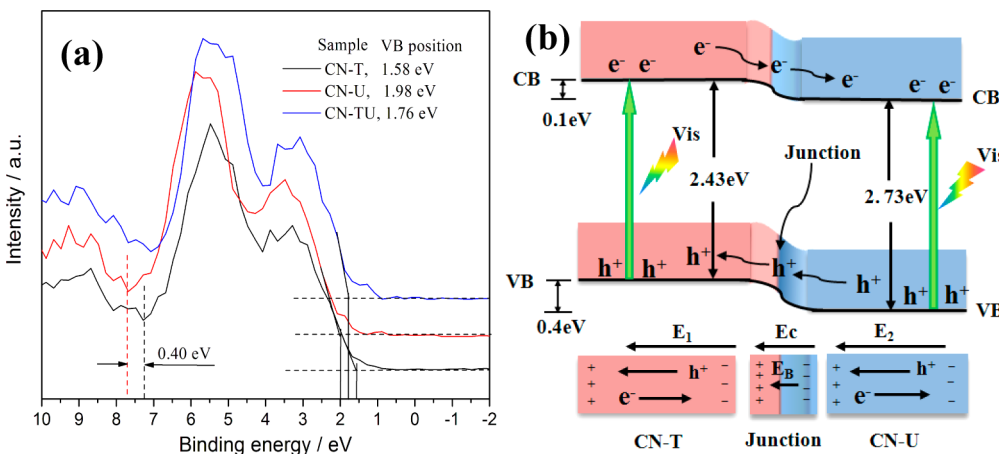


Figure 7. (a) VB XPS spectra of CN-T, CN-U, and CN-TU, and (b) schematic illustration of electron–hole separation and transport at the g-C₃N₄/g-C₃N₄ heterojunction interface and in both semiconductors: E_C is the contact electric field for the two components; E_B is the potential barrier in the interfacial depletion layer ($E_B < E_C$ during the photocatalytic reaction); E_1 and E_2 are the internal electric fields induced by the redistribution of the spatial charges in CN-T and CN-U, respectively.

3.3. Mechanism of CN-TU Metal-Free Heterojunction. The UV–vis DRS of CN-T, CN-U, and CN-TU are presented in Figure 6a. The optical absorption spectra reveal that all the samples feature an intrinsic semiconductor-like absorption in the blue region of the visible spectra. CN-T shows stronger absorption intensities compared to CT-U in visible light region due to the different degree of condensation with thiourea and urea. According to the SEM images, the average thickness of CN-T and CN-U sheets are 400–800 and 20–40 nm, respectively. The blue shift of band edge of CT-U by 0.28 eV compared to CN-T reflects the quantum confinement effects of the thermally induced thinner nanosheet structure as is evidenced in TEM (Figure 3b), because the size and thickness of CN-U are in nanoscale region compared with the big size and bulk structure of CN-T. The band edge of CN-TU is located between CN-T and CN-U, which further confirmed the electronic coupling of these two components in the CN-T/CN-U heterojunction. The band gap energy (E_g) estimated from the intercept of the tangents to the plots of $(\alpha h\nu)^{1/2}$ vs photon energy are 2.45, 2.73 eV for CN-T and CN-U respectively, as shown in the Figure 6b.^{32,52} The band gaps calculated herein are consistent with the literature values.^{30–32} The marked difference in band gap energy of g-C₃N₄ samples from thiourea and urea provide great potential for the design of g-C₃N₄-based isotype heterojunction with well-matched band structure.

The band structures of g-C₃N₄ samples from thiourea and urea were further examined by VB XPS as shown in Figure 7a. With VB XPS, the VB maxima of CN-T and CN-U are revealed to be 1.58 and 1.98 eV, respectively.^{48,49,54} The VB potential of CN-U is shown to be more positive than that of CN-T. With the band gap energies shown in Figure 6b, the CB position of CN-T and CN-U are calculated to be −0.85 and −0.75 eV, indicating that the CB potential of CN-T is more negative than that of CN-U. Table 1 summarizes the VB position, CB position, and band gap energy for CN-T, CN-U, and CN-TU samples.

On the basis of VB and CB levels of CN-T and CN-U, a band structure diagram for CN-T/CN-U phase heterojunction

Table 1. Determined VB Position, CB Position, Band Gap Energy, NO Removal Ratio, and Initial Reaction Constant for CN-T, CN-U, and CN-TU Samples

sample	VB position (eV)	CB position (eV)	band gap energy E_g (eV)	S_{BET} (m ² /g)	NO removal ratio η (%)	reaction constant k (min ⁻¹)
CN-T	1.58	−0.85	2.43	27	27.3	0.089
CN-U	1.98	−0.75	2.73	75	31.7	0.064
CN-TU	1.76	−0.82	2.60	41	47.6	0.151

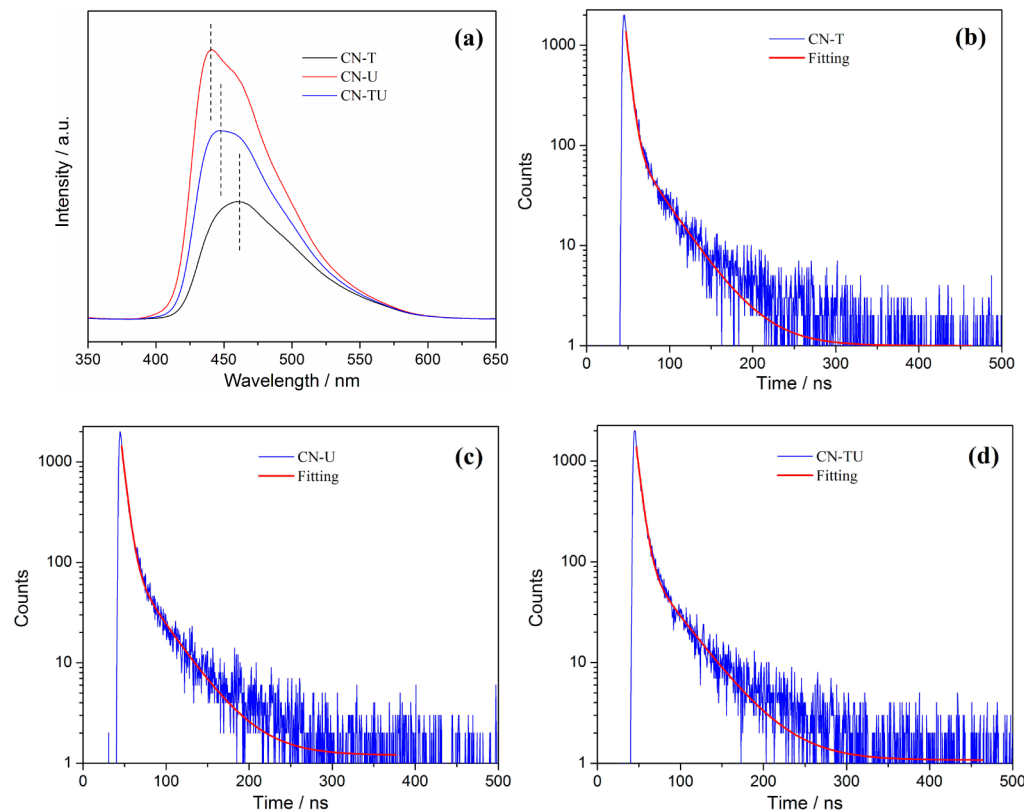


Figure 8. (a) Room-temperature PL spectra and (b–d) ns-level time-resolved PL spectra monitored at 450 nm under 420 nm excitation at 77 K for (b) CN-T, (c) CN-U, and (d) CN-TU.

can be drawn as shown in Figure 7b. As illustrated in Figure 7b, once CN-T and CN-U are electronically coupled together, the band alignment between the two kinds of $\text{g-C}_3\text{N}_4$ materials results in the formation of heterojunction with well-matched band structure.

Upon visible-light irradiation of CN-TU heterojunction, the photogenerated electrons tend to transfer from CN-T to CN-U driven by CB offset of 0.10 eV, whereas the photogenerated holes transfer from CN-U to CN-T driven by VB offset of 0.40 eV. The potential difference is the main driving force for efficient charge separation and transfer.^{49–51} These two charge transfer processes are beneficial for overcoming the high dissociation barrier of the Frenkel exciton and stabilizing electrons and holes. The redistribution of electrons on one side of the heterojunction (CN-U) and holes on the opposite side (CN-T), could reduce the electron/hole pairs recombination, which is an energy-wasteful process. The establishment of steady internal electric fields is also shown in Figure 7b. As the photogenerated electrons and holes are spatially separated into two different phases of $\text{g-C}_3\text{N}_4$, the charge recombination is drastically inhibited, which is of great benefit for enhancing the photocatalytic activity. In addition, with effective separation of electron/hole pairs, the lifetime of photogenerated charge carriers is expected to be prolonged. The prolonged lifetime allows the fast charge transfer to the reactive substrates on the photocatalyst surface, promoting the photocatalysis reaction.^{49–51}

3.4. Photoelectrochemical properties of $\text{g-C}_3\text{N}_4/\text{g-C}_3\text{N}_4$ heterojunction. PL emission spectra originating from the recombination of free charge carriers are useful to reveal the migration, transfer and separation of photogenerated charge carriers. Figure 8a shows that all the samples show one kind of

broad luminescence peak centered at around 450 nm with certain shift in peak position. This emission peak can be attributed to the radiative recombination of charge carriers. The shift of the peak position is consistent with variation of band gap energy of these samples (Figure 6b). The pristine CN-U has a strong PL emission peak. This energy-wasteful charge recombination process of CN-U can be greatly inhibited by coupling with the CN-T as a result of the redistribution of electrons in one side (CN-T) and holes in the other side (CN-U) driven by the band offsets. Thus, the intrinsic drawbacks of fast charge recombination in $\text{g-C}_3\text{N}_4$ have been solved by the construction of an isotype heterojunction, and a better photocatalytic performance of CN-TU can be expected. Note that the CN-T has a low PL emission peak, which is associated with its structural imperfection, as evidenced by XRD. The structural imperfection increased the number of structural defects (e.g., uncondensed $-\text{NH}_2$, $-\text{NH}$ groups), which could capture the electrons or holes, thus resulting in low radiative PL emission.^{32,55}

To understand the photophysical characteristics of photo-excited charge carriers, we recorded the ns-level time-resolved fluorescence decay spectra of CN-T, CN-U, and CN-TU, as shown in Figure 8b–d. By fitting the decay spectra, the radiative lifetimes with different percentages can be determined as given in Table 2. The short lifetime of CN-T and CN-U are 5.11 and 5.65 ns, respectively. The short lifetime is increased up to 5.85 ns in the CN-TU heterojunction. The long lifetime of charge carriers increase from 35.17 ns for CN-T and 35.75 ns for CN-U to 39.73 ns in the CN-TU heterojunction. These results mean that the radiative lifetime of all the charge carriers are increased by formation of $\text{g-C}_3\text{N}_4/\text{g-C}_3\text{N}_4$ heterojunction, which will play an important role in improving the probability

Table 2. Kinetics of Emission Decay Parameters of CN-T, CN-U, CN-TU Samples

samples	component	life time (ns)	relative percentage (%)	χ^2
CN-T	τ_1	5.11	64.94	1.064
	τ_2	35.17	35.06	
CN-U	τ_1	5.65	68.71	1.038
	τ_2	35.75	31.29	
CN-TU	τ_1	5.85	65.45	1.048
	τ_2	39.73	34.55	

of their involvement in photocatalytic reaction before recombination. The increased lifetime of charge carriers is associated with the enhanced charge transfer and electronic band structure coupling induced by the novel g-C₃N₄/g-C₃N₄ heterojunction.⁵⁵ This prolonged lifetime would lead to the increased probability of electrons or holes that are captured by reactive substrates to initiate the photocatalytic reactions.

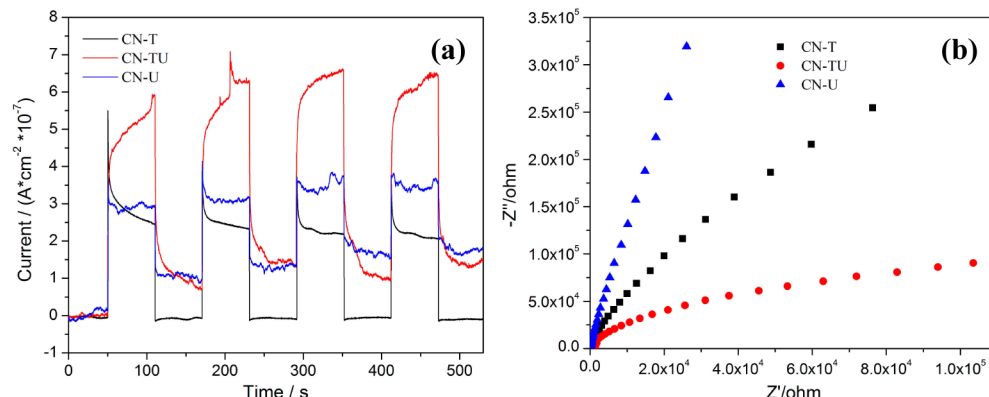
Photocurrents were measured for CN-T, CN-U, and CN-TU electrodes to investigate the electronic interaction between CN-T and CN-U, as shown in Figure 9a. It can be seen that fast photocurrent responses via on-off cycles were observed in these electrodes under visible-light irradiation, which may directly correlate with the separation efficiency of photo-generated carriers. The photocurrent of the CN-TU heterojunction electrode is significantly higher than that of CN-T and CN-U. The photocurrent enhancement of CN-TU heterojunction photocatalyst indicated an enhanced photoinduced separation of electron/hole pairs, which could be attributed to the formation of isotype g-C₃N₄/g-C₃N₄ heterojunction promoting the charges separation (Figure 7). This result was also consistent with time-resolved PL, which further confirmed the formation of g-C₃N₄/g-C₃N₄ heterojunction.

Furthermore, electrochemical impedance spectroscopy (EIS) was used to investigate the photogenerated charge separation process. EIS Nyquist plots of CN-T, CN-T,U and CN-U electrodes under visible light irradiation are shown in Figure 9b. A smaller arc radius of the EIS Nyquist plot suggests an effective separation of photogenerated electron–hole pairs and fast interfacial charge transfer.^{56,57} The arc radius on EIS Nyquist plot of CN-TU heterojunction is smaller than that of CN-T and CN-U. These results indicate the dramatically enhanced separation and transfer efficiency of electron–hole pairs in CN-TU because of the formation of this novel isotype g-C₃N₄/g-C₃N₄ heterojunction.

3.5. Visible light photocatalytic activity and stability for NO removal. The photocatalytic performance of all the samples was tested for removal of NO in air under visible-light irradiation in a continuous reactor. Reference experiments showed that NO could not be photolyzed when the reactor was illuminated in the absence of a photocatalyst or in the presence of the photocatalyst without illumination. Figure 10a shows the variation of NO concentration (C/C_0 %) with irradiation time over the samples. All g-C₃N₄ samples show decent visible light photocatalytic activity for NO removal. After irradiation for 30 min, the NO removal ratio of CN-T and CN-U was 27.3 and 31.7%, respectively. But dramatically, CN-TU exhibited an enhanced NO removal ratio of 47.6% compared to host substrates of CN-T and CN-U. The initial reaction constants of the samples are shown in Table 1. To further underline the importance of intimate coupling for heterojunction, the physical mixture sample of CN-T and CN-U were also tested. No significant enhancement could be observed in Figure 10a. This result suggested that the physical mixture of CN-T and CN-U failed to produce close electronic contact between CN-T and CN-U. For comparison, the g-C₃N₄/g-C₃N₄ composites from solid state composite of thiourea and urea were prepared under the same thermal treatment conditions. The result indicated that the photocatalytic activity of the g-C₃N₄/g-C₃N₄ composites was slightly enhanced with a removal ratio of 37.4%. However, it is much lower than that of the g-C₃N₄/g-C₃N₄ heterojunction (47.6%) prepared from molecular composite precursors of thiourea and urea, demonstrating the great merits of employing the molecular composite precursors.

To determine the stability of the CN-TU heterojunction as visible-light photocatalyst, we carried out repeated consecutive experiments and the result is shown in Figure 10b. It can be seen that the CN-TU heterojunction is able to maintain a high NO removal ratio under repeated irradiation without noticeable deactivation.

The surface areas of CN-T, CN-U, and CT-TU are observed to be 27, 75, and 41 m²/g, respectively. Obviously, the surface areas do not play a significant role in enhancing the photocatalytic activity of CT-TU as the CN-U sample with the highest surface areas had a low activity (Table 1). On the other side, The CN-T sample with the strongest visible light absorption also exhibited low activity. These facts further confirm that the enhanced photocatalytic performance of CN-TU was promoted by the generation of isotype heterojunction that greatly separated the charge carriers (Figure 8a and Figure

**Figure 9.** Photoresponses (a) and Nyquist plots for CN-T, CN-TU, and CN-U electrodes under visible light irradiation ($\lambda > 420$ nm, $[Na_2SO_4] = 0.5$ M).

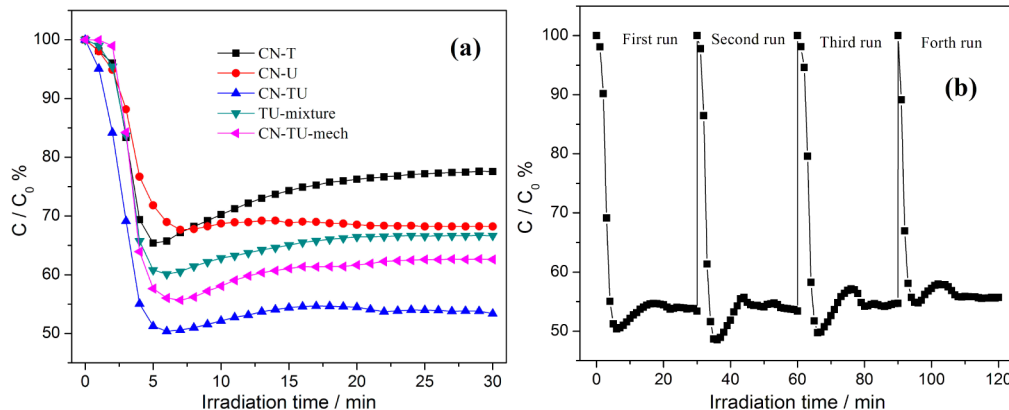


Figure 10. (a) Visible-light photocatalytic performance of CN-T, CN-U, CN-TU, CN-mixture, and CN-TU-Mech samples for removal NO in air and (b) multiple photocatalytic reaction over CN-TU, (continuous reactor, NO concentration: 600 ppb).

9) and prolonged the lifetime of the charge carriers (Figure 8b).^{49–51} The strategy of the facile in situ construction of isotype heterojunction could be extended to design other metal-free heterostructures for enhanced performance. The CN-TU metal-free heterojunction is also expected to be applied widely in other related areas of solar energy conversion, organic photosynthesis, and photovoltaic devices.

4. CONCLUSION

In conclusion, CN-T/CN-U metal-free isotype heterojunction was constructed in situ with molecular composite precursors based on the band alignment between CN-T and CN-U. Using easily available green precursors of thiourea and urea, this synthesis method is facile, economic, and environmentally benign. The differences in electronic band structures of CN-T and CN-U make the CB and VB levels match with each other. This novel metal-free isotype heterojunction was demonstrated to promote charge separation and prolong the lifetime of charge carriers driven by the band offsets, resulting in a significant enhancement in the photocatalytic activity for NO removal under visible light irradiation. The isotype heterostructure strategy developed herein could provide new perspectives for sustainable utilization of solar irradiation by using earth-abundant precursors and constructing other layered polymeric heterostructures to promote charge separation for high-performance photocatalysis. The nanostructured layered g-C₃N₄/g-C₃N₄ heterojunction can also be envisaged to be applied in other related areas, such as solar energy conversion, photosynthesis, and photovoltaic devices.

ASSOCIATED CONTENT

Supporting Information

SEM images of CN-T and CN-U are shown in Figure S1, and FT-IR spectra of CN-T, CN-U and CN-TU are shown in Figure S2. This material is available free of charge via the Internet at <http://pubs.acs.org>.

AUTHOR INFORMATION

Corresponding Author

*Tel/Fax: + 23-62769785-605. E-mail: dfctbu@126.com.

Notes

The authors declare no competing financial interest.

ACKNOWLEDGMENTS

This research is financially supported by the National Natural Science Foundation of China (51108487), the Natural Science Foundation Project of CQ CSTC (cstc2012jjA20014, cstc2013jcyjA20018, cstc2013yykfB50008), the Science and Technology Project from Chongqing Education Commission (KJ130725), the Innovative Research Team Development Program in University of Chongqing (KJTD201314, KJTD201020), the Opening Project of Key Laboratory of Green Catalysis of Sichuan Institutes of High Education (LZJ1204). The research was also supported by research grant of Early Career Scheme (ECS 809813) from the Research Grant Council, Hong Kong SAR Government and Internal Research Grant (R3429), and the internal research grant (RG77/12-13R) and start-up research grant (RG73/12-13R) from The Hong Kong Institute of Education. The authors thank Dr. Ying Zhou and Ziyan Zhao in Southwest Petroleum University for the measurement of photocurrent and EIS.

REFERENCES

- Chen, C. C.; Ma, W. H.; Zhao, J. C. *Chem. Soc. Rev.* **2010**, *39*, 4206–4219.
- Xiang, Q. J.; Yu, J. G.; Jaroniec, M. *Chem. Soc. Rev.* **2012**, *41*, 782–796.
- Tong, H.; Ouyang, S. X.; Bi, Y. P.; Umezawa, N.; Oshikiri, M.; Ye, J. H. *Adv. Mater.* **2011**, *24*, 229.
- Liu, S. W.; Yu, J. G.; Jaroniec, M. *Chem. Mater.* **2011**, *23*, 4085–4093.
- Di Paola, A.; García-López, E.; Marci, G.; Palmisano, L. *J. Hazard. Mater.* **2012**, *211–212*, 3–29.
- Wang, Y.; Wang, X. C.; Antonietti, M. *Angew. Chem., Int. Ed.* **2012**, *51*, 68–89.
- Wang, X. C.; Blechert, S.; Antonietti, M. *ACS Catal.* **2012**, *2*, 1596–1606.
- Zheng, Y.; Liu, J.; Liang, J.; Jaroniec, M.; Qiao, S. *Energy Environ. Sci.* **2012**, *5*, 6717–6731.
- Devi, L. G.; Kavitha, R. *Appl. Catal., B* **2013**, *140–141*, 559–587.
- Liu, G.; Niu, P.; Cheng, H. M. *ChemPhysChem* **2013**, *14*, 885–892.
- Liu, G.; Niu, P.; Sun, C.; Smith, S. C.; Chen, Z.; Lu, G.; Cheng, H. *J. Am. Chem. Soc.* **2010**, *132*, 11642–11648.
- Dong, F.; Wang, H. Q.; Wu, Z. B.; Qiu, J. F. *J. Colloid Interface Sci.* **2010**, *343*, 200–208.
- Dong, F.; Ho, W. K.; Lee, S. C.; Wu, Z. B.; Fu, M.; Zou, S. C.; Huang, Y. *J. Mater. Chem.* **2011**, *21*, 12428–12436.
- Dong, F.; Sun, Y. J.; Ho, W. K.; Wu, Z. B. *Dalton Trans.* **2012**, *41*, 8270–8284.

- (15) Liu, Z.; Wu, B.; Zhu, Y.; Wang, F.; Wang, L. *J. Colloid Interface Sci.* **2013**, *392*, 337–380.
- (16) Hou, J.; Cao, R.; Wang, Z.; Jiao, S.; Zhu, H. *J. Hazard. Mater.* **2012**, *217–218*, 177–186.
- (17) Dong, F.; Sun, Y. J.; Fu, M.; Wu, Z. B.; Lee, S. C. *J. Hazard. Mater.* **2012**, *219–220*, 26–34.
- (18) Dong, F.; Sun, Y. J.; Fu, M.; Ho, W. K.; Lee, S. C.; Wu, Z. B. *Langmuir* **2012**, *28*, 766–773.
- (19) Wang, P.; Huang, B. B.; Dai, Y.; Whangbo, M. H. *Phys. Chem. Chem. Phys.* **2012**, *14*, 9813–9826.
- (20) Yu, J. G.; Dai, G. P.; Huang, B. B. *J. Phys. Chem. C* **2009**, *113*, 16394–16401.
- (21) Wang, X. C.; Maeda, K.; Thomas, A.; Takanabe, K.; Xin, G.; Carlsson, J. M.; Domen, K.; Antonietti, M. *Nat. Mater.* **2009**, *8*, 76–80.
- (22) Wang, F.; Ng, W. K. H.; Yu, C. J.; Zhu, H. J.; Li, C. H.; Zhang, L.; Liu, Z. F.; Li, Q. *Appl. Catal., B* **2012**, *111*, 409–414.
- (23) Liu, G.; Niu, P.; Yin, L. C.; Cheng, H. M. *J. Am. Chem. Soc.* **2012**, *134*, 9070–9073.
- (24) Hong, J. D.; Xia, X. Y.; Wang, Y. S.; Xu, R. *J. Mater. Chem.* **2012**, *30*, 15006–15012.
- (25) Liu, Y.; Chen, G.; Zhou, C.; Hu, Y.; Fu, D.; Liu, J.; Wang, Q. *J. Hazard. Mater.* **2011**, *190*, 75–80.
- (26) Zhang, J.; Sun, J.; Maeda, K.; Domen, K.; Liu, P.; Antonietti, M.; Fu, X. Z.; Wang, X. C. *Energy Environ. Sci.* **2011**, *4*, 675–678.
- (27) Zhang, J. H.; Zhang, M. W.; Zhang, G. G.; Wang, X. C. *ACS Catal.* **2012**, *2*, 940–948.
- (28) Zhang, J. S.; Chen, X. F.; Takanabe, K.; Maeda, K.; Domen, K.; Epping, J. D.; Fu, X. Z.; Antonietti, M.; Wang, X. C. *Angew. Chem., Int. Ed.* **2010**, *49*, 441–444.
- (29) Bojdys, M. J.; Müller, J.; Antonietti, M.; Thomas, A. *Chem.—Eur. J.* **2008**, *14*, 8177–8182.
- (30) Dong, F.; Wu, L. W.; Sun, Y. J.; Fu, M.; Wu, Z. B.; Lee, S. C. *J. Mater. Chem.* **2011**, *21*, 15171–15174.
- (31) Dong, F.; Sun, Y. J.; Wu, L. W.; Fu, M.; Wu, Z. B. *Catal. Sci. Technol.* **2012**, *2*, 1332–1335.
- (32) Dong, F.; Wang, Z. Y.; Sun, Y. J.; Ho, W. K.; Zhang, H. D. *J. Colloid Interface Sci.* **2013**, *401*, 70–79.
- (33) Cui, Y. J.; Zhang, J. S.; Zhang, G. G.; Huang, J. H.; Liu, P.; Antonietti, M.; Wang, X. C. *J. Mater. Chem.* **2011**, *21*, 13032–13039.
- (34) Xu, J.; Wu, H. T.; Wang, X.; Xue, B.; Li, Y. X.; Cao, Y. *Phys. Chem. Chem. Phys.* **2013**, *15*, 4510–4517.
- (35) Cui, Y. J.; Ding, Z. X.; Fu, X. Z.; Wang, X. C. *Angew. Chem., Int. Ed.* **2012**, *51*, 11814–11818.
- (36) Lin, Z. Z.; Wang, X. C. *Angew. Chem., Int. Ed.* **2013**, *52*, 1735–1738.
- (37) Xiang, Q. J.; Yu, J. G.; Jaroniec, M. *J. Phys. Chem. C* **2011**, *115*, 7355–7363.
- (38) Hou, Y. D.; Laursen, A. B.; Zhang, J. S.; Zhang, G. G.; Zhu, Y. S.; Wang, X. C.; Dahl, S.; Chorkendorff, I. *Angew. Chem., Int. Ed.* **2013**, *52*, 1–6.
- (39) Yan, H. J.; Yang, H. X. *J. Alloys Compd.* **2011**, *509*, 26–29.
- (40) Yan, S. C.; Lv, S. B.; Li, Z. S.; Zou, Z. G. *Dalton. Trans.* **2010**, *39*, 1488–1491.
- (41) Sun, J. X.; Yuan, Y. P.; Qiu, L. G.; Jiang, X.; Xie, A. J.; Shen, Y. H.; Zhu, J. F. *Dalton. Trans.* **2012**, *41*, 6756–6763.
- (42) Wang, Y. J.; Bai, X. J.; Pan, C. S.; He, J.; Zhu, Y. F. *J. Mater. Chem.* **2012**, *22*, 11568–11573.
- (43) Cheng, N.; Tian, J.; Liu, Q.; Ge, C.; Qusti, A. H.; Asiri, A. M.; Al-Youbi, A. O.; Sun, X. *ACS Appl. Mater. Interfaces* **2013**, *5*, 6815–6819.
- (44) Fu, J.; Chang, B. B.; Tian, Y. L.; Xi, F. N.; Dong, X. P. *J. Mater. Chem. A* **2013**, *1*, 3083–3090.
- (45) Huang, L.; Xu, H.; Li, Y.; Cheng, X.; Xia, J.; Cai, G. *Dalton. Trans.* **2013**, *42*, 8606–8616.
- (46) Tian, Y. L.; Chang, B. B.; Lu, J. L.; Fu, J.; Xi, F. N.; Dong, X. P. *ACS Appl. Mater. Interfaces* **2013**, *5*, 7079–7085.
- (47) Zhang, J.; Xu, Q.; Feng, Z. C.; Li, M. J.; Li, C. *Angew. Chem., Int. Ed.* **2008**, *47*, 1766–1769.
- (48) Scanlon, D. O.; Dunnill, C. W.; Buckeridge, J.; Shevlin, S. A.; Logsdail, A. J.; Woodley, S. M.; Catlow, C. R. A.; Powell, M. J.; Palgrave, R. G.; Parkin, I. P.; Watson, G. W.; Keal, T. W.; Sherwood, P.; Walsh, A.; Sokol, A. A. *Nat. Mater.* **2013**, *12*, 798–801.
- (49) Wang, X.; Xu, Q.; Li, M.; Shen, S.; Wang, X.; Wang, Y.; Feng, Z.; Shi, J.; Han, H.; Li, C. *Angew. Chem., Int. Ed.* **2012**, *51*, 13089–13092.
- (50) Hou, J.; Yang, C.; Wang, Z.; Zhou, W.; Jiao, S.; Zhu, H. *Appl. Catal., B* **2013**, *142–143*, 504–511.
- (51) Zhang, J. S.; Zhang, M. W.; Sun, R. Q.; Wang, X. C. *Angew. Chem., Int. Ed.* **2012**, *51*, 10145–10149.
- (52) Zhang, G. G.; Zhang, J. S.; Zhang, M. W.; Wang, X. C. *J. Mater. Chem.* **2012**, *22*, 8083–8091.
- (53) Sing, K. S. W.; Everett, D. H.; Haul, R. A. W.; Moscou, L.; Pierotti, R. A.; Rouquerol, J.; Siemieniewska, T. *Pure Appl. Chem.* **1985**, *57*, 603–619.
- (54) Chu, S.; Wang, Y.; Guo, Y.; Feng, J.; Wang, C.; Luo, W.; Fan, X.; Zou, Z. G. *ACS Catal.* **2013**, *3*, 912–919.
- (55) Niu, P.; Zhang, L.; Liu, G.; Cheng, H. M. *Adv. Funct. Mater.* **2012**, *22*, 4763–4770.
- (56) Zhou, Y.; Zhang, Q.; Li, Y. H.; Antonova, E.; Bensch, W.; Patzke, G. R. *Sci. China Chem.* **2013**, *56*, 435–442.
- (57) Bai, X.; Wang, L.; Zong, R.; Zhu, Y. *J. Phys. Chem. C* **2013**, *117*, 9952–9961.